Nonlinear Relationships of Fibrin Network Structure as a Function of Fibrinogen and Thrombin Concentrations for Purified Fibrinogen and Plasma Clots

Can Cai[1]*, Zezhong Zhang[1]*, Arezoo Nameny[1], Keith Bonin[1], Brittany Bannish[2], Nathan E. Hudson[3], Glen Marrs[4], Stephen Baker[1†], Martin Guthold[1†]

[1] Department of Physics, Wake Forest University, Winston-Salem, NC 27109

[2] Department of Mathematics and Statistics, University of Central Oklahoma, Edmond, Oklahoma, 73034

[3] Department of Physics, East Carolina University, Greenville, NC 27885

[4] Department of Biology, Wake Forest University, Winston-Salem, NC 27109

* These authors contributed equally to this work.

[†.] These authors are co-corresponding authors of this article.

Abstract

Background. Fibrinogen levels are linked to bleeding disorders and thrombotic disease. Thrombin converts fibrinogen to fibrin, producing the load bearing fibrin scaffold that determines clot mechanical and transport properties.

Objective. Quantitatively determine how fibrinogen and thrombin concentrations affect fibrin network architecture in human plasma and in purified Peak 1 fibrinogen.

Methods. Single fiber dimensions were quantified by scanning electron microscopy, measuring fiber diameter and branch-to-branch segment length using a standardized sample preparation protocol. Network structure was quantified by confocal microscopy, measuring fiber density and pore size using a standardized acquisition and analysis workflow.

Results and Conclusions. Across both plasma clots and purified fibrinogen clots, all metrics were well described by compact, empirical power law relationships of the form $Y = k[Fgn]^{\alpha}[Thr]^{\beta}$, yielding predictive equations that link composition to structure. Increasing thrombin decreased fiber diameter and segment length, whereas increasing fibrinogen increased diameter and had comparatively weak influence on segment length. At the network scale, increasing fibrinogen or thrombin increased fiber density and reduced pore size, with fibrinogen exerting the stronger effect on these metrics. For the same fibrinogen and thrombin concentrations, purified fibrinogen clots formed denser networks with smaller pores than plasma clots, with thinner and shorter fibers. Together, these results provide a quantitative framework for forecasting fibrin structure from fibrinogen and thrombin concentrations across plasma and purified fibrinogen clot preparations.

Introduction

Blood clotting is a tightly regulated in space and time: clots must assemble rapidly and locally at sites of vascular injury to prevent blood loss, seal the wound, and limit infection. In bleeding disorders such as hemophilia and von Willebrand disease, impaired fibrin formation or platelet adhesion can yield delayed, undersized, mechanically weak clots that may fail to arrest bleeding. When clotting is initiated inappropriately or fails to undergo timely fibrinolysis, persistent thrombi in critical vascular beds such as the brain, heart, and deep veins can lead to ischemic stroke, myocardial infarction, and deep vein thrombosis. [1,2]

Fibrin fibers provide the load bearing scaffold of the clot. In the prevailing assembly model, thrombin cleaves fibrinopeptides A and B to expose binding sites termed ‘knob A’ and

‘knob B’ that drive knob-hole interactions, forming half staggered protofibrils that elongate by end addition and thicken by lateral aggregation, a process influenced by the alpha C regions. [1] As these bundles intersect, they form a branched, three-dimensional network. Abnormal fibrinogen levels are clinically relevant: elevated fibrinogen is associated with ischemic stroke, myocardial infarction, and venous thromboembolism, whereas reduced fibrinogen, for example in postpartum hemorrhage, predisposes to bleeding. [3–5] Thrombin generation is likewise central: insufficient thrombin, as in some types of hemophilia, causes hemostatic failure, while excessive or sustained thrombin, as in cancer associated thrombosis or antiphospholipid syndrome, promotes thrombosis. [6–8] Together, fibrinogen and thrombin set the structural state of the network, which in turn shapes clot mechanical behavior and susceptibility to lysis. [1]

A persistent challenge is that published structure concentration relationships are difficult to compare across studies, even when the qualitative conclusions appear similar. For fiber diameter, most reports spanning confocal microscopy, SEM, and turbidimetry support an increase with fibrinogen, whereas a smaller set report the opposite trend. [10–14] Reported diameters also span a wide range, from tens of nanometers to micrometers. [11–14] This variability is not solely biological. It reflects differences in measurement resolution and in the analysis and modeling frameworks used to map concentration to structure. Confocal microscopy is diffraction limited and cannot resolve fiber diameters under about 200 nm. [9] SEM provides higher spatial resolution, but sample preparation steps such as washing, dehydration, and coating can alter apparent geometry. [10,12,13,14] Light scattering relies on models that use approximations and can be less accurate when fibers are very thin or become very thick (on the order of the wavelength of light) or networks are highly

heterogeneous. [11] As a result, studies have described diameter dependence using different functional forms, including approximately linear relations in some SEM analyses [13] and nonlinear scaling consistent with power law behavior in scattering-based work. [11] In contrast to the fibrinogen dependence, there is broader agreement that increasing thrombin produces thinner fibers, although the reported magnitude again varies across methods. [10,12–14]

Fiber length and pore scale metrics add further complexity because they are intrinsically harder to define and measure in images. Fiber segments commonly extend beyond the field of view, and apparent crossings in two-dimensional projections do not always correspond to true branch points, complicating segmentation and length assignment. [16] A prior confocal study quantified apparent lengths from single planes and reported shorter apparent lengths with increasing fibrinogen or thrombin. [13] However, a growing body of work indicates that structural features such as fiber diameter and length are not well described by normal distributions, motivating robust summary statistics and careful aggregation across images. [10, 17–18] For example, a standardized SEM study reported lognormal diameter distributions, [18] and three-dimensional confocal reconstructions indicate lognormal like behavior for both diameter and length. [10] For network packing, fiber density has been estimated from confocal images using intensity-based measures [13] and from light scattering through inference of structural parameters. [11] Pore size is often quantified from confocal data using a largest inscribed circle or bubble analysis that yields a pore diameter distribution, [20] alongside alternative estimators such as chord length intercepts or distance map-based approaches. [19] Across these approaches, a consistent

qualitative trend is that higher fibrinogen or thrombin tends to reduce pore size, although the reported functional form varies between datasets and analysis choices. [13,20–22]

Despite extensive prior work describing how fibrinogen and thrombin influence fibrin network architecture, the field still lacks a predictive and quantitatively transferable mapping from composition to structure that spans multiple structural metrics and can be reused across studies. In practice, most reports emphasize qualitative trends (e.g., thicker versus thinner fibers) or provide method- and pipeline-specific absolute values that are difficult to reconcile because definitions, resolution limits, and preparation/analysis workflows differ. This limits mechanistic inference and modeling: without internally consistent scaling relationships for fiber diameter, segment-level length, network density, and pore size, it remains difficult to (i) test assembly hypotheses, (ii) link microstructure to mechanics and fibrinolysis, or (iii) calibrate and validate multiscale simulations of clot structure, mechanics, and transport.

Here we test the hypothesis that fibrin architecture across a fibrinogen–thrombin condition matrix follows a common *nonlinear scaling* form that can be expressed compactly by power-law relationships. We place plasma and purified systems on the same biochemical coordinate system (fibrinogen × thrombin), enabling direct cross-system comparisons and revealing a robust system-dependent shift in the scaling prefactor k, consistent with plasma-dependent modulation of the baseline microstructural scale at fixed $[Fg]$ and $[Thr]$. We combine standardized, high-magnification SEM [18] to quantify fiber diameter and segment-level length with 3D confocal imaging to quantify fiber density and pore size (line-intercept crossing counts and slice-wise bubble analysis [20]). Using a shared power-law parameterization across metrics and systems, we derive a unified set of

scaling equations that functions as a practical "structure calculator" for predicting network morphology and provides quantitative benchmarks for testing mechanistic assembly models and for validating computational simulations of fibrin and related fibrous hydrogels.

Materials & Methods

Reagents

Pooled normal human plasma (George King Bio-Medical, Product #0010) and Peak 1 human fibrinogen (Enzyme Research Laboratories, Cat# P1 FIB) were aliquoted and stored at −80 °C. Human thrombin (Enzyme Research Laboratories, Cat# HT1002a) was aliquoted and stored at −80 °C. Alexa Fluor 488–conjugated human fibrinogen (Thermo Fisher Scientific, Cat# F13191) was aliquoted and stored at −80 °C. Aliquots were thawed at 37 °C immediately before use.

SEM sample preparation and imaging

Clot conditions. Plasma clots were prepared at room temperature across a 4×4 matrix of fibrinogen (0.36, 0.73, 1.45, 2.9 mg/mL) and thrombin (0.05, 0.1, 0.2, 1.0 U/mL). Purified (Peak 1) clots were prepared across a 3×3 matrix of fibrinogen (0.36, 0.73, 1.45 mg/mL) and thrombin (0.05, 0.1, 0.2 U/mL). Clotting was initiated by adding an activation mix containing thrombin and $CaCl_2$ to achieve final concentrations of 20 mM $CaCl_2$ and the thrombin concentrations listed above in Tris-buffered saline (50 mM Tris, 100 mM NaCl, pH 7.4). Clots were allowed to polymerize for 2 h at room temperature.

Fixation, drying, and coating. Samples were prepared using a standardized wash–fix–dehydrate–dry workflow as previously described [18]. After polymerization, clots formed in Eppendorf tube lids were washed three times in sodium cacodylate buffer (50 mM sodium cacodylate, 100 mM NaCl) and then fixed by immersion in 2 mL of 2% glutaraldehyde prepared in the same buffer for 6 h. Following fixation, samples were washed three additional times in sodium cacodylate buffer, dehydrated through a graded ethanol series (30%-100%), and dried using hexamethyldisilazane (HMDS). Dried samples were sputter-coated with gold for 45 s (Cressington Model 108).

SEM imaging. Samples were imaged on a Zeiss Gemini 300 SEM under high vacuum at 30,000× magnification. For each condition, 16 images (randomly selected fields of view) were collected.

Confocal sample preparation and imaging

Clot conditions and sample preparation. For confocal experiments, plasma clots and purified fibrinogen (Peak 1) fibrin clots were prepared using a 3×3 matrix of fibrinogen (0.36, 0.73, and 1.45 mg/mL) and thrombin (0.05, 0.1, and 0.2 U/mL) in TBS (20 mM Tris, 150 mM NaCl, pH 7.4) with 20 mM $CaCl_2$. Alexa Fluor 488–fibrinogen was incorporated at 6.5% of the total fibrinogen concentration. Immediately before use, the labeled fibrinogen was warmed and briefly centrifuged (10 s) to remove aggregates. Reactions were loaded into channel slides (ibidi μ-Slide VI 0.4), shielded from light, and allowed to polymerize for 2 h at room temperature.

Confocal imaging. Imaging was carried out on a Zeiss LSM 710 laser-scanning confocal microscope with a 40× oil-immersion objective using 488 nm excitation light. For each

condition, 36 z-stacks were collected (18 per slide from two slides). Each slide contained six channels; three imaging positions per channel were selected at random, spaced several millimeters apart and positioned 3–6 μm away from channel edges to reduce boundary effects. Stacks spanned 212 μm × 212 μm in x–y and 15 μm in z (33 optical sections, 0.47 μm step size) and were acquired at 8-bit depth. Detector gain was tuned to clearly resolve fibers while minimizing background signal.

Image analysis and quantitative network metrics

Fiber diameter. An ImageJ-based manual approach was used to quantify fiber diameter. Briefly, an evenly spaced grid was overlaid on each image, and fibers intersecting (or closest to) each grid crossing were selected for measurement, ensuring that each fiber was measured only once. At least 70 fibers were measured per image.

Fiber length. Using the grid-sampling method described above, fiber length was traced in ImageJ and defined as the distance along a fiber segment between adjacent branch points. To avoid including truncated segments near the field boundaries, measurements were taken only within an interior region of interest defined by excluding a 10% margin from each image edge (i.e., fibers were measured only if they lay ≥10% of the image width/height away from the boundaries), while using the original, unaltered images. This corresponds to sampling the central 64% of the field of view. At least 30 fibers were measured per image.

Fiber density. Image stacks were converted into 2D maximum-intensity projections in ImageJ, followed by binarization. Twenty horizontal and twenty vertical equidistant lines were superimposed on each image and the number of fibers intersecting each line was counted. Fiber density was quantified from maximum-intensity projections as the mean

number of fibrin fibers crossing a 100 μm line. Because each maximum projection was generated from a 15 μm z-stack, each 100 μm line effectively samples fibers within a 100 μm (length) × 15 μm (depth) region; therefore, fiber density is reported as the number of fibers per 1500 μm^2. A 15 μm acquisition depth provided images with a high number of clearly resolvable, predominantly straight fibers and minimal background fluorescence. While the maximum projection can, in principle, lead to a slight undercount at the highest fibrinogen/thrombin conditions due to occasional overlap, fibers were generally well separated and readily distinguishable across conditions.

Bubble analysis

Individual z-slices were exported as multi-page TIFFs and binarized in MATLAB using a threshold set to three times the mean slice intensity. Fiber-free pores were quantified with a custom algorithm that places the largest possible circles ("bubbles") within void regions on each slice, as described in [10]. Circles that touched fibers, overlapped with larger accepted circles, or intersected the image boundary were discarded. The diameters of the remaining circles were recorded as a proxy for network porosity, where larger bubble diameters indicate larger pore/void regions.

Curve fitting and statistical analysis

For each experimental condition, image-level measurements were summarized and related to the two experimental factors—fibrinogen concentration [Fgn] and thrombin concentration [Thr]—using a power-law model:

$$Y = k\,[\mathrm{Fgn}]^{\alpha}[\mathrm{Thr}]^{\beta},$$

where Y denotes the response variable (fiber diameter, fiber length, fiber density, or bubble diameter) and k, α, and β are fitted parameters. Model fitting was performed in log space by linear regression of

$$\ln(Y) = \ln(k) + \alpha \ln([Fgn]) + \beta \ln([Thr]),$$

using ordinary least squares (OLS). Goodness of fit was reported as R^2 computed in log space. Parameter uncertainty was quantified by 95% confidence intervals, and two-sided hypothesis tests were used to assess whether k, α and β differed from zero.

Because the distributions of fiber diameter, fiber length, and bubble diameter were non-Gaussian, these responses were summarized per condition using the median of image-level medians prior to model fitting. In contrast, fiber density was approximately normally distributed and was summarized per condition using the mean of image-level means prior to fitting.

Results

Purified (Peak 1) and plasma clots show distinct architectures across matched concentration matrices

Across the fibrinogen–thrombin matrices, SEM and confocal imaging reveal systematic changes in fibrin network architecture. Under comparable conditions, purified (Peak 1) clots form denser networks with smaller pores than plasma clots (Figs. 1 and 2), even though their fibers are thinner and shorter (Figs. 4 and 5). Overall, fibrinogen more strongly modulates fiber density and pore size, whereas thrombin more strongly influences fiber

diameter and length. These differences are evident throughout the condition space rather than being driven by a single corner condition.

Power law fits quantify how fibrinogen and thrombin shape fibers and pores. To quantify concentration dependence, each structural metric was fit with a power law $Y = k[Fgn]^{\alpha}[Thr]^{\beta}$ (Figs. 3 and 6; Table 1 and 2). The resulting exponents capture distinct contributions of fibrinogen and thrombin in both plasma and Peak 1 systems.

Fiber diameter (SEM). Fiber diameter increases with fibrinogen concentration and decreases with thrombin concentration in both plasma and Peak 1 clots. The same directional dependence is observed in both systems.

Fiber length (SEM). Fiber length shows a strong dependence on thrombin (shorter segments at higher thrombin) but weak sensitivity to fibrinogen. Consistent with this, the fitted fibrinogen exponent for length is small in both plasma and purified systems ($\alpha < 0.1$; Tables 1 and 2), yielding an almost flat trend versus fibrinogen compared with the thrombin dependence.

Fiber density and pore size (confocal). Confocal analysis showed that fiber density increases with both fibrinogen and thrombin, with fibrinogen having the stronger influence (Tables 1 and 2). In parallel, bubble diameter decreased with increasing fibrinogen and thrombin, indicating smaller pore spaces at higher concentrations.

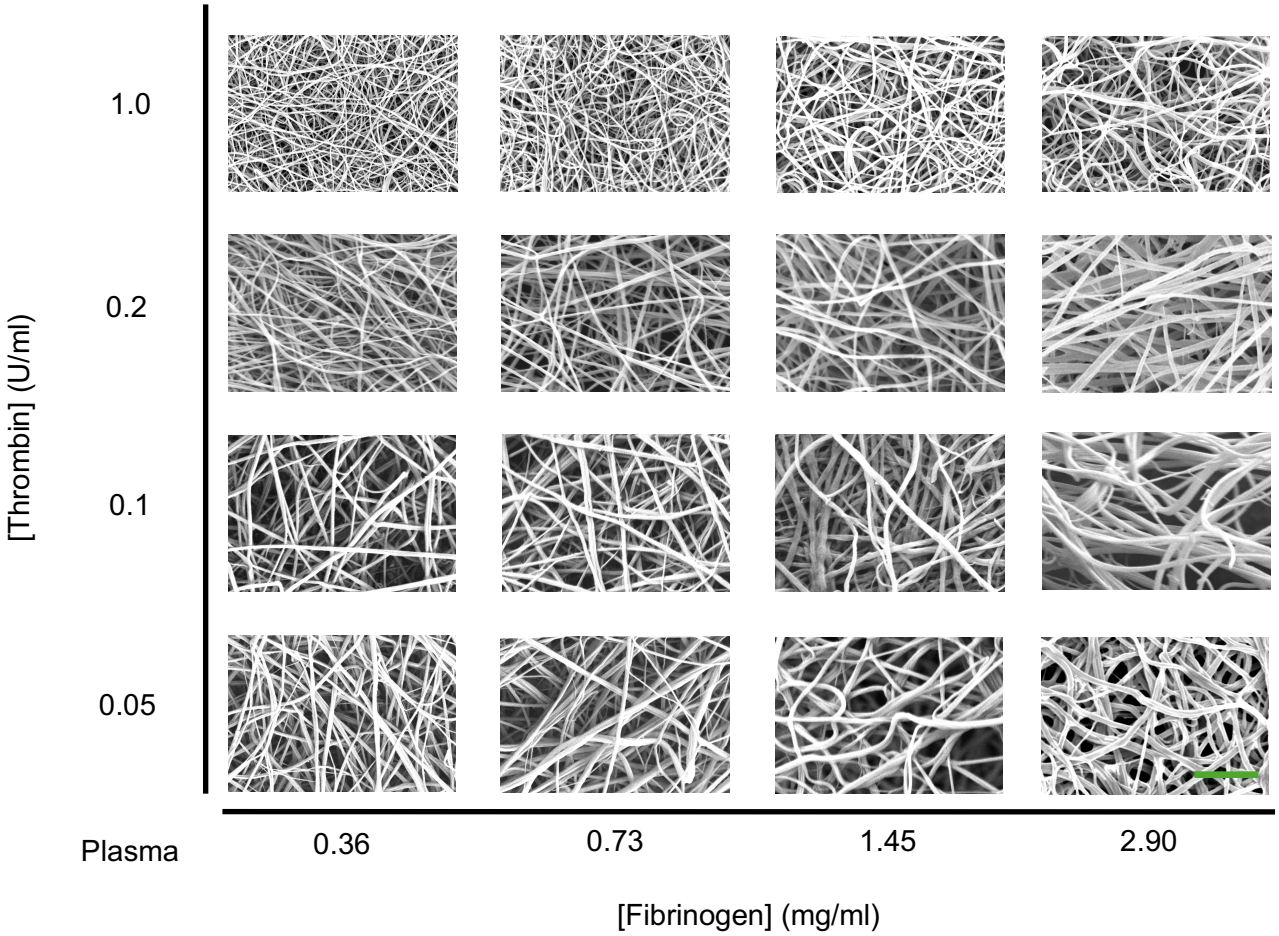

Figure 1: 4×4 matrix of representative SEM images showing plasma fibrin network structure across fibrinogen (x-axis) and thrombin (y-axis) concentrations. Each panel corresponds to a specific fibrinogen–thrombin condition. Scale bar: 1 µm.

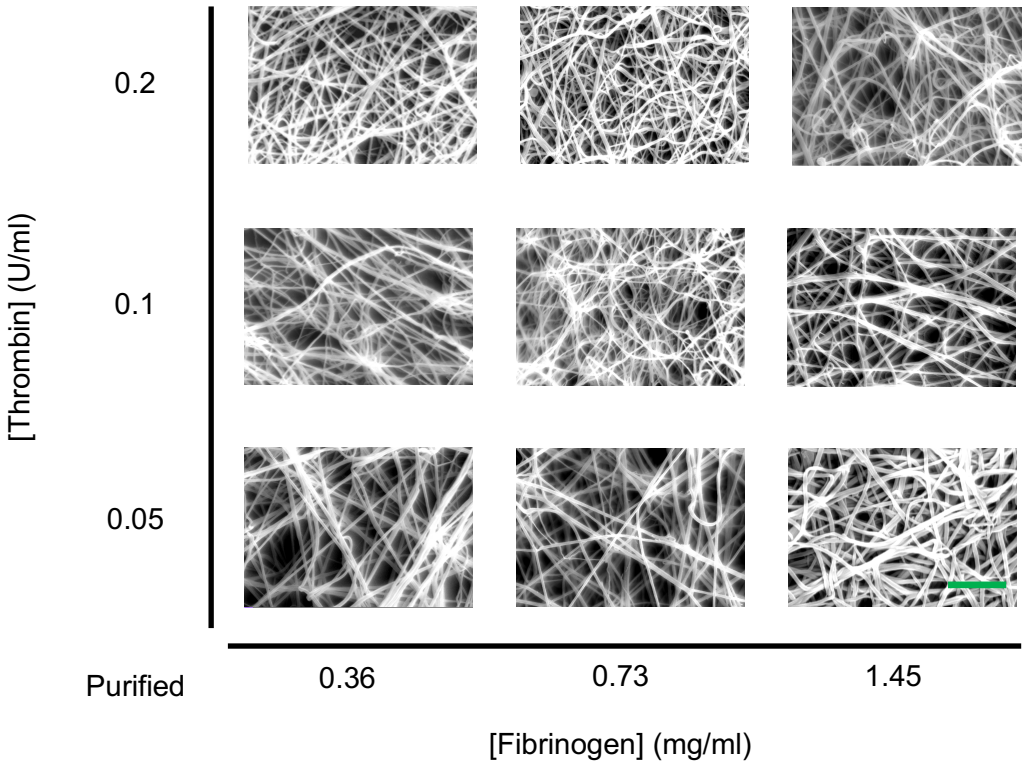

Figure 2: 3×3 matrix of representative SEM images showing purified (Peak 1) fibrin network structure across fibrinogen (x-axis) and thrombin (y-axis) concentrations. Each panel corresponds to a specific fibrinogen–thrombin condition. Scale bar: 1 µm.

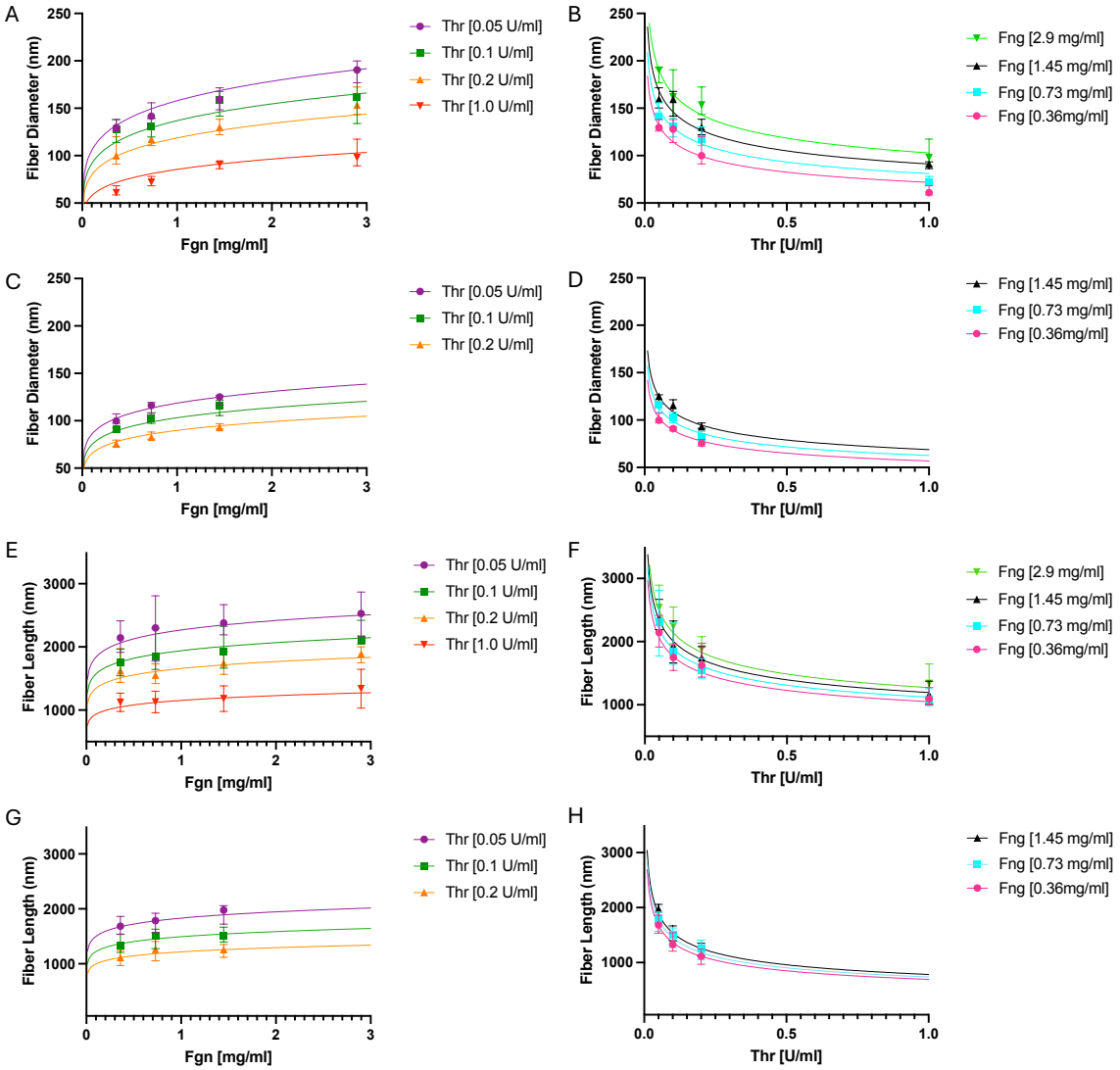

Figure 3: Concentration trends of fiber diameter and fiber length measured from SEM images, with power law fits. For each condition, fiber diameter and fiber length were summarized by the median. Solid lines indicate power law fits. Error bars show 95% confidence intervals across images within each condition. (A,B) Plasma fiber diameter vs fibrinogen and thrombin. (C,D) Purified (Peak 1) fiber diameter vs fibrinogen and thrombin. (E,F) Plasma fiber length vs fibrinogen and thrombin. (G,H) Purified (Peak 1) fiber length vs fibrinogen and thrombin.

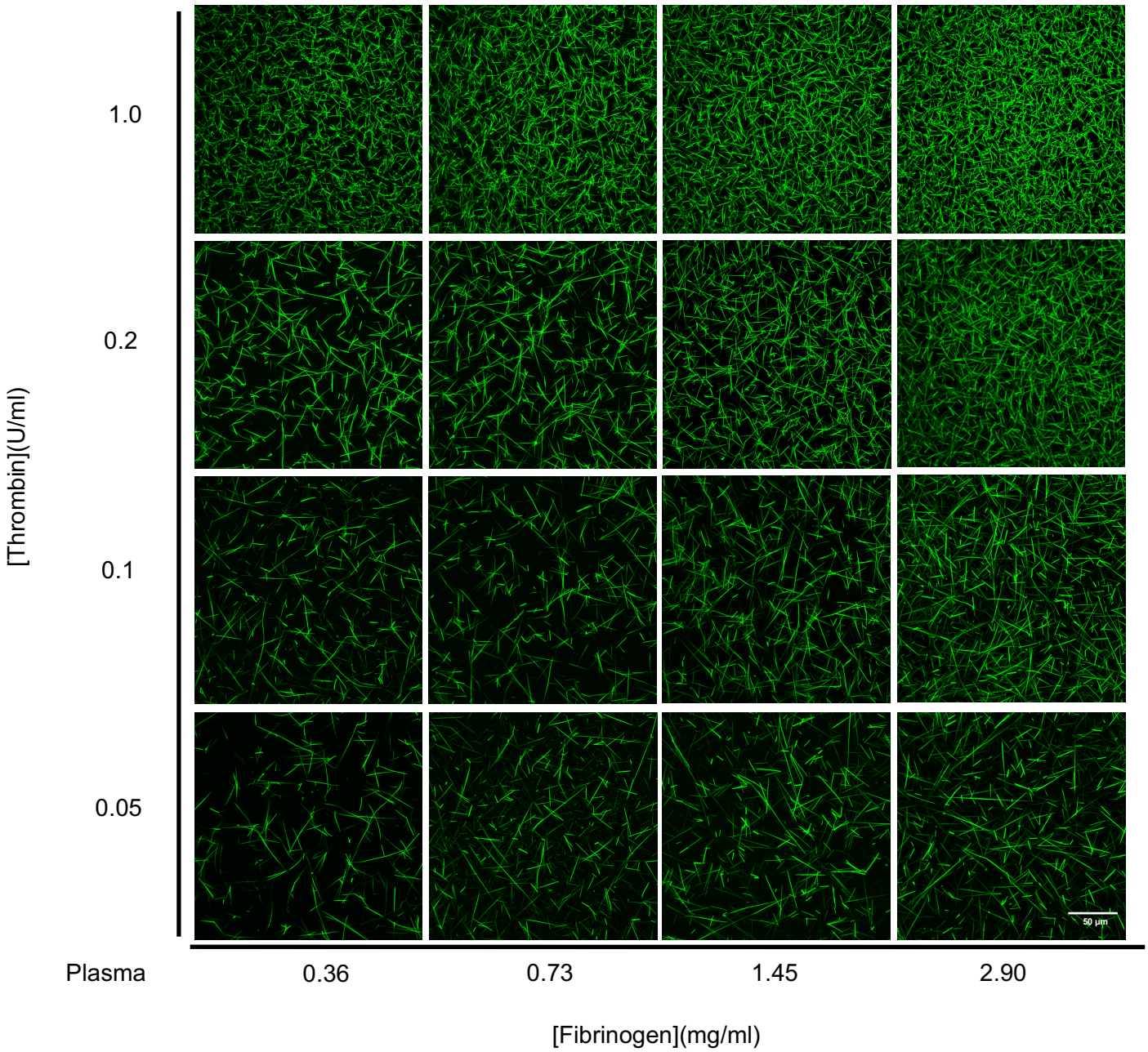

Figure 4: 4×4 matrix of representative confocal images showing plasma fibrin network structure across fibrinogen (x-axis) and thrombin (y-axis) concentrations. Each panel corresponds to a specific fibrinogen–thrombin condition. Scale bar: 50 µm.

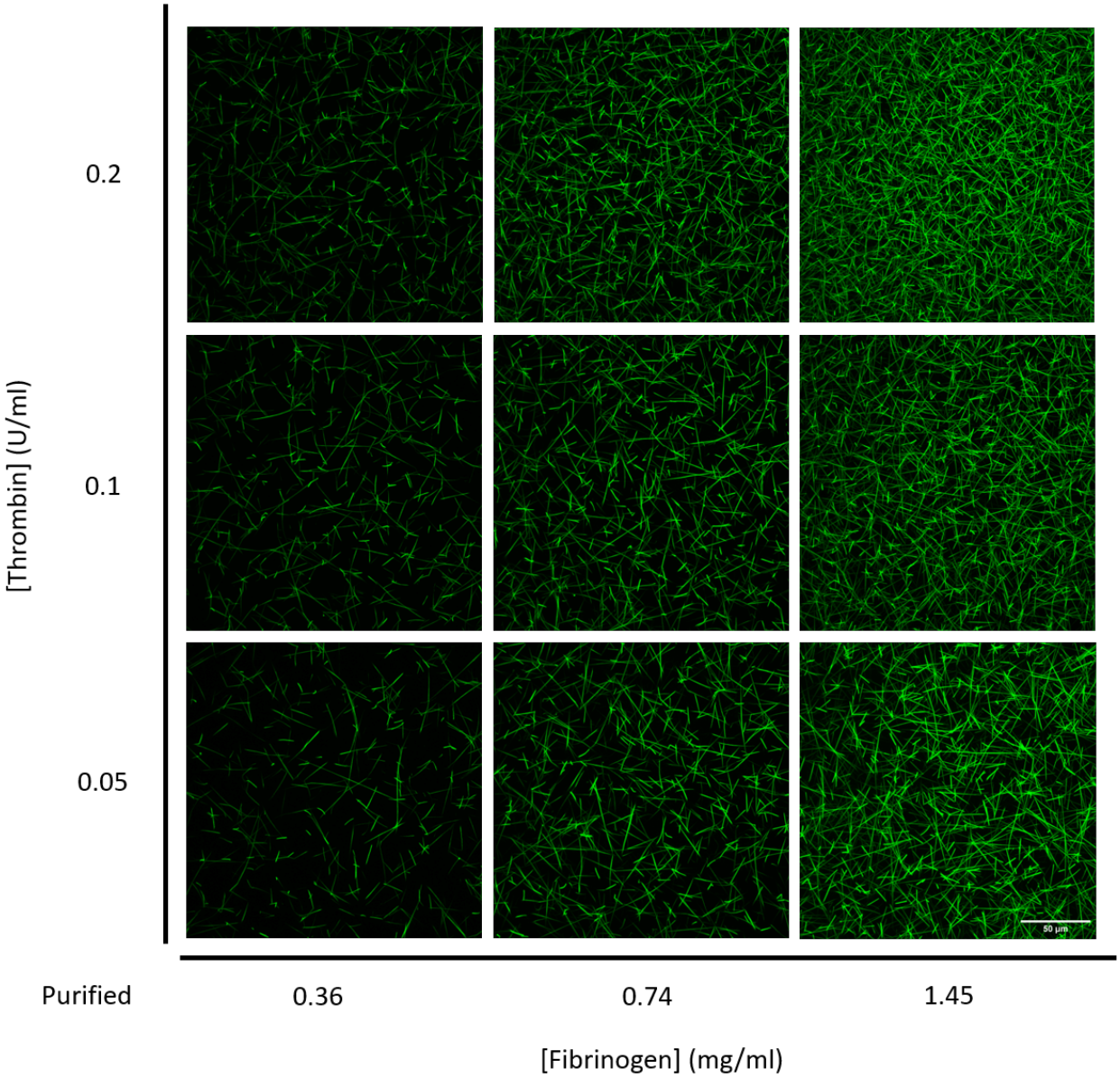

Figure5: 3×3 matrix of representative confocal images showing purified (Peak 1) fibrin network structure across fibrinogen (x-axis) and thrombin (y-axis) concentrations. Each panel corresponds to a specific fibrinogen–thrombin condition. Scale bar: 50 µm.

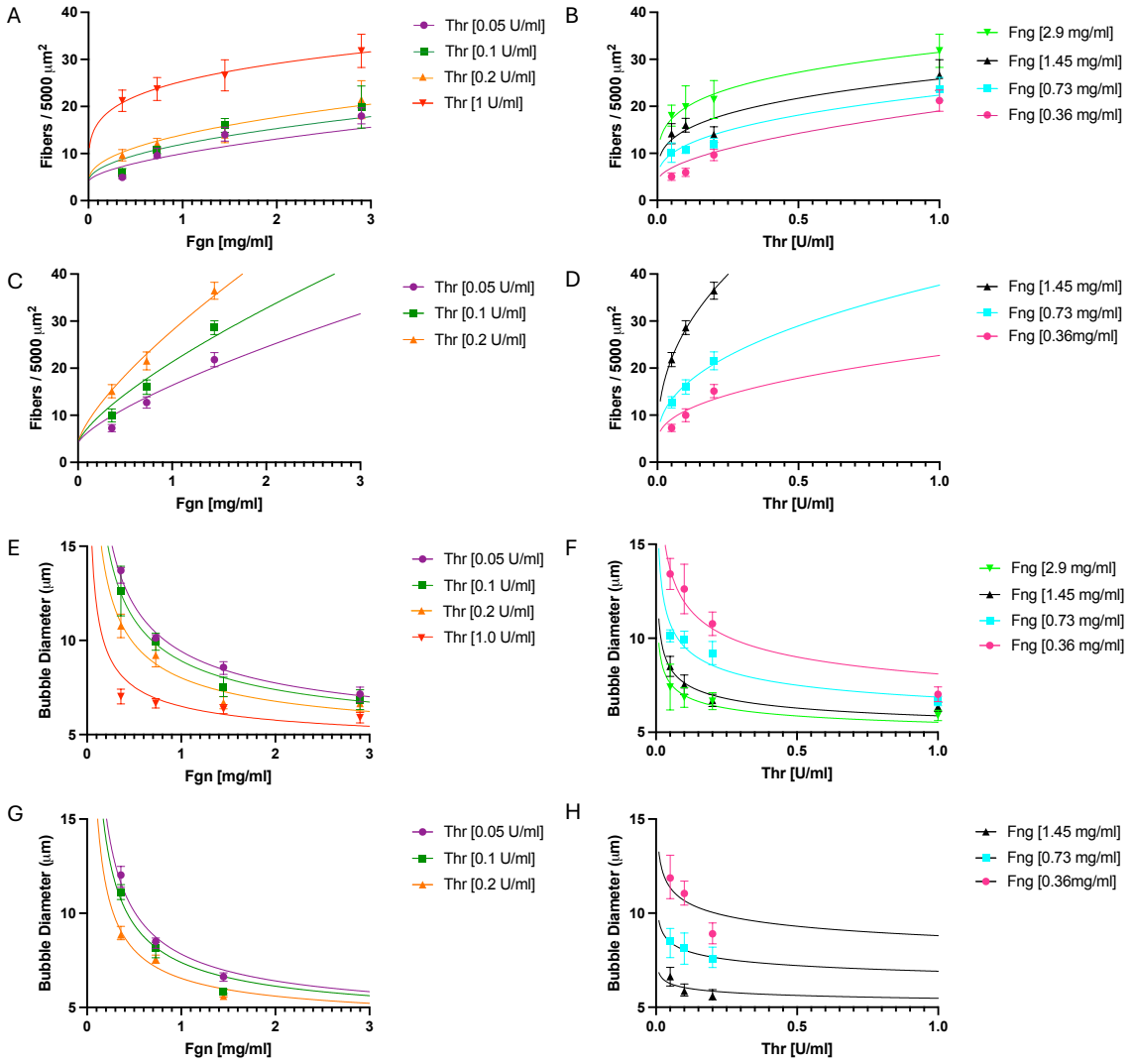

Figure 6: Concentration trends of fiber count and bubble diameter measured from confocal images, with power law fits. For each condition, fiber count was summarized by the mean, whereas bubble diameter was summarized by the median. Solid lines indicate power law fits. Error bars show 95% confidence intervals across images within each condition. (A,B) Plasma fiber count vs fibrinogen and thrombin. (C,D) Purified (Peak 1) fiber count vs fibrinogen and thrombin. (E,F) Plasma bubble diameter vs fibrinogen and thrombin. (G,H) Purified (Peak 1) bubble diameter vs fibrinogen and thrombin.

Plasma		Value	95% CI	P-Value	R^2 (log)
Parameters for Fiber diameter	k	81.20	[75.88, 86.65]	4.55e-22	0.95867
	α	0.19	[0.14, 0.24]	9.79e-7	
	β	- 0.23	[-0.26, -0.20]	1.30e-9	
Parameters for Fiber length	k	1154.51	[1065.74, 1249.03]	2.80e-12	0.96107
	α	0.092	[0.062, 0.12]	4.71e-5	
	β	-0.24	[-0.30, -0.17]	4.55e-5	
Parameters for Fiber density	k	25.09	[20.61, 30.56]	5.56e-09	0.88230
	α	0.45	[0.32, 0.59]	1.90e-05	
	β	0.30	[0.21, 0.40]	1.52e-03	
Parameters for Bubble diameter	k	6.57	[5.99, 7.20]	1.56e-15	0.88995
	α	-0.24	[-0.30, -0.17]	2.48e-06	
	β	-0.14	[-0.18, 0.091]	1.98e-05	

Table 1: Power-law fit parameters and statistical results for plasma fiber diameter, fiber length, fiber density, and bubble diameter using the model $Y = k\,[Fgn]^{\alpha}[Thr]^{\beta}$.

Purified Fibrinogen		Value	95% CI	P-Value	R^2 (log)
Parameters for Fiber diameter	k	63.65	[56.09, 72.22]	2.48e-10	0.95928
	α	0.15	[0.09, 0.20]	4.86e-4	
	β	- 0.21	[-0.26, -0.16]	6.74e-5	
Parameters for Fiber length	k	774.52	[571.60, 1049.24]	1.08e-5	0.84395
	α	0.071	[0.026, 0.12]	5.75e-3	
	β	-0.29	[-0.42, -0.16]	8.38e-3	
Parameters for Fiber density	k	56.67	[45.80, 70.14]	6.76e-09	0.98895
	α	0.73	[0.64, 0.81]	1.01e-06	
	β	0.43	[0.34, 0.52]	2.36e-05	
Parameters for Bubble diameter	k	5.06	[4.26, 6.02]	4.46e-7	0.97270
	α	-0.41	[-0.48, -0.33]	8.98e-06	
	β	-0.14	[-0.22, 0.070]	2.94e-03	

Table 2: Power-law fit parameters and statistical results for purified fiber diameter, fiber length, fiber density, and bubble diameter using the model $Y = k\,[Fgn]^{\alpha}[Thr]^{\beta}$.

Discussion

Justification for power law fitting

We used the empirical form $Y = k[Fgn]^{\alpha}[Thr]^{\beta}$ because power law scaling follows from a minimal mass action plus allocation argument. As a concrete example, we will consider the fiber diameter d.

Let $A(t)$ denote the effective pool of assembly competent fibrin species produced during thrombin cleavage. During polymerization, both substrate and enzyme activities decrease with time, so we allow time dependent effective concentrations, often well approximated by exponential decays: $[Fgn]_{eff}(t)$. A compact representation is

$$\frac{dA}{dt} \propto [Fgn]_{eff}(t)\,[Thr].$$

Let $N(t)$ be the number density of effective growing units (independently growing protofibril or early fiber starts). The net formation rate of such units is commonly written [25] as

$$\frac{dN}{dt} \propto A(t)^{m},$$

where m is an effective reaction order that captures the rate limiting association pathway (it need not be 2 and need not be an integer).

Integrating over an early assembly window t_g yields a multiplicative scaling

$$N \propto [Fgn]^{q}[Thr]^{p},$$

where p and q absorb both the kinetic order and the time integrals of the decaying effective concentrations.

Fiber diameter then follows from distributing fibrin mass across these growing units. In a fixed imaging volume, the fibrin mass incorporated into fibers scales with the starting fibrinogen level (for simplicity, we assume the internal fiber mass density is homogeneous here), $V_{fiber} \propto [Fgn]$. Geometrically,

$$V_{fiber} \propto N\, d^2\, \ell,$$

where ℓ is an effective length contributed per growing unit (allowed to depend on [Fgn] and [Thr]). Combining gives

$$d \propto \left(\frac{[Fgn]}{N\,\ell}\right)^{1/2}.$$

If ℓ itself scales as a power law, $\ell \propto [Fgn]^u [Thr]^v$ (or varies weakly enough to be absorbed into fitted exponents), then substituting $N \propto [Fgn]^q [Thr]^p$ yields

$$d \propto [Fgn]^{\frac{1-q-u}{2}} [Thr]^{-\frac{p+v}{2}} \equiv k\, [Fgn]^{\alpha} [Thr]^{\beta}.$$

Thus, even with time dependent reagent depletion and without specifying microscopic details, a power law dependence arises generically from mass action driven production of assembly competent species, an effective nucleation step that sets the density of growing units, and geometric allocation of fibrin mass among those units.

Conserved concentration sensitivities with environment-dependent scaling (plasma vs purified system)

Across plasma and purified systems, the fitted power-law exponents are similar, indicating that the structural sensitivities to [Fgn] and [Thr] are largely conserved and consistent with a shared underlying assembly mechanism across our condition matrix. In contrast, the prefactor k shifts substantially between systems. Because Ca^{2+} and NaCl concentrations were matched, a simple explanation might be reduced effective thrombin activity in plasma due to thrombin consumption and inhibition (e.g., antithrombin, with contributions from α2-macroglobulin and heparin cofactor II). Consistent with an attenuated effective thrombin-catalyzed assembly drive in plasma, a turbidity study [13] reported markedly faster polymerization kinetics in purified fibrinogen than in plasma under comparable nominal conditions. Interpreting the k-shift as a simple rescaling of thrombin activity yields an estimate that $[\mathrm{Thr}]_{\mathrm{eff}}$ may be reduced by ~65–80% in plasma.

Kinetic control (thrombin) vs space-filling control (fibrinogen)

Our scaling analysis exposes a hierarchical division of labor between thrombin and fibrinogen: thrombin primarily sets the gelation dynamics and thus the effective growth window for individual fibers, whereas fibrinogen primarily sets how the network fills space within the imaged thickness. Mechanistically, increasing thrombin accelerates cleavage and early assembly, effectively increasing the rate at which assembly-competent species and growing starts ("seeds") are generated. A higher seed density means protofibrils and early fibers encounter and connect with each other sooner, thereby advancing the percolation/gel point and truncating the time available for continued elongation of any single fiber. Consistent with this kinetic picture, fiber length is overwhelmingly thrombin-set—doubling thrombin shortens length by ~15% in plasma (2^-0.24 ≈ 0.85) and ~18% in

purified/peak1 ($2^{-0.29} \approx 0.82$), while doubling fibrinogen changes length by only ~5–7% ($2^{0.071}$–$2^{0.092} \approx 1.05$–1.07)—arguing that elongation is time-limited by thrombin-controlled progression to connectivity rather than monomer-limited. In the same framework, a larger number of starts naturally yields a denser projected network, and the faster kinetic partitioning of a finite material supply among more growing units biases fibers toward being slightly thinner; indeed, projected fiber density increases with thrombin ($\beta \approx 0.30$ in plasma; $\beta \approx 0.43$ in purified/peak1), while fiber diameter decreases modestly with thrombin ($\beta \approx -0.23$ and -0.21, respectively).

In contrast, fibrinogen strongly reprograms the projected space-filling architecture: doubling fibrinogen increases projected fiber density by ~37% in plasma ($2^{0.45} \approx 1.37$) and ~66% in purified/peak1 ($2^{0.73} \approx 1.66$), while reducing the projected void scale quantified by bubble diameter by ~15% in plasma ($2^{-0.24} \approx 0.85$) and ~25% in purified/peak1 ($2^{-0.41} \approx 0.75$), respectively; thrombin's effect on bubble diameter is comparatively small (~9% per doubling; $2^{-0.14} \approx 0.91$ in both systems). Notably, the fibrinogen exponent for bubble diameter is approximately half (with opposite sign) of the fibrinogen exponent for projected density in both systems ($-0.24/0.45 \approx -0.53$; $-0.41/0.73 \approx -0.56$), implying a near-geometric packing relation bubble $\propto$ density$^{-1/2}$ in our 2D maximum projection readout. The weaker density–fibrinogen scaling in plasma ($\alpha \approx 0.45$ vs 0.73) likely reflects that additional plasma constituents and regulation can partially mask a purely material-limited response in this projection-based metric; a similar buffering may contribute to the weaker bubble–fibrinogen scaling in plasma ($\alpha \approx -0.24$ vs -0.41). In the purified system, the mapping from available fibrinogen to projected occupancy appears more direct, yielding a steeper exponent. Finally, fiber diameter is only weakly and oppositely tuned—fibrinogen slightly thickens (~+11–14%

per doubling) while thrombin slightly thins (~−14–15% per doubling)—so these effects can largely cancel, yielding a weak net diameter dependence even as packing and projected void geometry shift dramatically.

Volume-allocation check supports fibrinogen-driven space filling

A useful internal consistency check is to combine our power-law scalings for fiber density, diameter, and length to estimate the fiber volume fraction in the imaged region, $\phi \equiv V_{\text{fibrin}}/V_{\text{image}}$. Fiber density is measured as a 2D count per area, ρ_{2D} (fibers/1500 μm^2). Under an isotropic spacing picture, the in-plane spacing scales as $s \sim \rho_{2D}^{-1/2}$; treating this spacing as the characteristic 3D territory per fiber gives $\rho_{3D} \propto s^{-3} \propto \rho_{2D}^{3/2}$. The minimal allocation relation is therefore $V_{\text{fibrin}} \propto \rho_{2D}^{3/2} d^2 l$, which implies $\alpha_V \approx \frac{3}{2}\alpha_\rho + 2\alpha_d + \alpha_l$ and $\beta_V \approx \frac{3}{2}\beta_\rho + 2\beta_d + \beta_l$. Using the fitted exponents gives $\alpha_V = 1.147$ and $\beta_V = -0.25$ in plasma, and $\alpha_V = 1.466$ and $\beta_V = -0.07$ in purified fibrinogen. If increasing fibrinogen only increased fiber volume at fixed fiber density, one would expect $\alpha_V \approx 1$. Instead, $\alpha_V > 1$ is consistent with fibrinogen driving a shift toward thicker fibers accompanied by reduced fiber density, as we observed previously [26]. In contrast, β_V is close to zero in purified, supporting the idea that thrombin mainly redistributes morphology/partitioning rather than increasing the total fiber volume fraction. The more negative plasma value is consistent with our highest-thrombin condition (1 U/mL)

producing very thin, highly crowded fibers, where overlap and finite confocal resolution can lead to undercounting of ρ_{2D}, which is amplified by the $\rho_{2D}^{3/2}$ mapping.

Thrombin sets a segment-length scale via seed density

Using the measured thrombin activity (3044 NIH U/mg) to convert nominal thrombin (NIH U/mL) into an approximate molecular concentration (~9 nM per 1 NIH U/mL), we tested a "one thrombin–one center" segmentation picture in which each active thrombin molecule seeds one effective growth center and sets one characteristic fiber segment. Under an isotropic spacing assumption, the characteristic segment scale follows the diagonal of an average cube, with $L_{\mathrm{seg}} \sim L_{\mathrm{cube}} \propto [\mathrm{Thr}]^{-1/3}$. This mapping predicts $L_{\mathrm{cube}} \approx 2.65, 2.12, 1.68$ and 0.98μm at 0.05, 0.1, 0.2, and 1 U/mL, respectively. The measured medians show the same thrombin-controlled contraction, with fibrinogen exerting only a minor modulation on length. In plasma (16 conditions), median length spans 2.14–2.53 μm at 0.05 U/mL, 1.75–2.12 μm at 0.1 U/mL, 1.55–1.89 μm at 0.2 U/mL, and 1.09–1.30 μm at 1 U/mL. To compare directly with the cube model (which depends only on thrombin), we summarize each thrombin level by the mean of the fibrinogen-specific medians; the plasma summaries are ~2.34, 1.91, 1.70, and 1.16 μm, tracking the cube-diagonal values closely over 0.05–0.2 U/mL and remaining on the predicted ~1 μm scale at 1 U/mL. In purified fibrinogen (9 conditions), the same trend holds but with a uniformly shorter absolute scale: medians are 1.69/1.79/1.98 μm (Fgn 0.36/0.73/1.45 mg/mL) at 0.05 U/mL, 1.33/1.51/1.52 μm at 0.1 U/mL, and 1.11/1.26/1.26 μm at 0.2 U/mL; the corresponding summaries are ~1.82, 1.45, and 1.21 μm. Together, these data support a simple geometric interpretation: increasing thrombin increases the density of independent growth centers, assigns each segment a smaller effective "cube," and compresses the growth window

before segments encounter one another and lock in connectivity—thereby shortening fibers/segments—while fibrinogen primarily redistributes material into space-filling outputs rather than extending the characteristic segment length.

Conclusion

Fibrinogen and thrombin jointly determine the structure of the fibrin fiber scaffold that governs clot mechanics and transport, yet their coupled effects on network architecture remain difficult to predict. Here we mapped fibrin structure across fibrinogen and thrombin concentration matrices in human plasma and purified Peak 1 fibrinogen. Scanning electron microscopy quantified fiber diameter and branch to branch segment length, and confocal microscopy quantified fiber density and pore size using standardized workflows. All readouts were captured by compact power law models $Y = k[Fgn]^{\alpha}[Thr]^{\beta}$, yielding fitted parameters that separate fibrinogen and thrombin contributions and enable direct prediction of architecture from composition. These parameterized scaling relations provide a quantitative foundation for mechanistic theory development and for interpreting how clinically relevant shifts in fibrinogen or thrombin may reshape clot microstructure.

References

1. Weisel JW, Litvinov RI. Mechanisms of fibrin polymerization and clinical implications. Blood. 2013;121(10):1712-1719. doi:10.1182/blood-2012-09-306639.
2. Undas A, Ariëns RAS. Fibrin clot structure and function: a role in the pathophysiology of arterial and venous thromboembolic diseases. Arterioscler Thromb Vasc Biol. 2011;31(12):e88-e99. doi:10.1161/ATVBAHA.111.230631.
3. Fibrinogen Studies Collaboration; Danesh J, et al. Plasma fibrinogen level and the risk of major cardiovascular diseases and nonvascular mortality: an individual participant meta-analysis. JAMA. 2005;294(14):1799-1809. doi:10.1001/jama.294.14.1799.
4. Klovaite J, Nordestgaard BG, Tybjærg-Hansen A, Benn M. Elevated fibrinogen levels are associated with risk of pulmonary embolism, but not with deep venous

thrombosis. Am J Respir Crit Care Med. 2013;187(3):286-293. doi:10.1164/rccm.201207-1232OC.
5. Charbit B, et al. The decrease of fibrinogen is an early predictor of the severity of postpartum hemorrhage. J Thromb Haemost. 2007;5(2):266-273. doi:10.1111/j.1538-7836.2007.02297.x.
6. Sidonio RF Jr, Hoffman M, Kenet G, Dargaud Y. Thrombin generation and implications for hemophilia therapies: a narrative review. Res Pract Thromb Haemost. 2023;7(1):100018. doi:10.1016/j.rpth.2022.100018.
7. Reddel CJ, Tan CW, Chen VM. Thrombin generation and cancer: contributors and consequences. Cancers (Basel). 2019;11(1):100. doi:10.3390/cancers11010100.
8. Gehlen R, Vandevelde A, de Laat B, Devreese KMJ. Application of the thrombin generation assay in patients with antiphospholipid syndrome: a systematic review of the literature. Front Cardiovasc Med. 2023;10:1075121. doi:10.3389/fcvm.2023.1075121.
9. Pietsch K, Storm-Johannsen L, Schmidt-Thomée A, Pompe T. Correlation between fibrin fibrillation kinetics and the resulting fibrin network microstructure. Adv Healthc Mater. 2023;12(8):e2202231. doi:10.1002/adhm.202202231.
10. Ryan EA, Mockros LF, Weisel JW, Lorand L. Structural origins of fibrin clot rheology. Biophys J. 1999;77(5):2813-2826. doi:10.1016/S0006-3495(99)77113-4.
11. Ferri F, Greco M, Arcòvito G, De Spirito M, Rocco M. Structure of fibrin gels studied by elastic light scattering techniques: dependence of fractal dimension, gel crossover length, fiber diameter, and fiber density on monomer concentration. Phys Rev E. 2002;66(1 Pt 1):011913. doi:10.1103/PhysRevE.66.011913.
12. Belcher HA, Guthold M, Hudson NE. What is the diameter of a fibrin fiber? Res Pract Thromb Haemost. 2023;7(5):100285. doi:10.1016/j.rpth.2023.100285.
13. Risman RA, Belcher HA, Ramanujam RK, et al. Comprehensive analysis of the role of fibrinogen and thrombin in clot formation and structure for plasma and purified fibrinogen. Biomolecules. 2024;14(2):230. doi:10.3390/biom14020230.
14. Weisel JW. Structure of fibrin: impact on clot stability. J Thromb Haemost. 2007;5(suppl 1):116-124. doi:10.1111/j.1538-7836.2007.02504.x.
15. Rowe SL, Lee S, Stegemann JP. Influence of thrombin concentration on the mechanical and morphological properties of cell-seeded fibrin hydrogels. Acta Biomater. 2007;3(1):59-67. doi:10.1016/j.actbio.2006.08.006.
16. Weisel JW, Nagaswami C. Computer modeling of fibrin polymerization kinetics correlated with electron microscope and turbidity observations: clot structure and assembly are kinetically controlled. Biophys J. 1992;63(1):111-128. doi:10.1016/S0006-3495(92)81594-1.
17. Kim OV, Litvinov RI, Weisel JW, Alber MS. Structural basis for the nonlinear mechanics of fibrin networks under compression. Biomaterials. 2014;35(25):6739-6749. doi:10.1016/j.biomaterials.2014.04.056.
18. Cai C, De Lange-Loots Z, Baker SR, et al. Standardization of scanning electron microscopy analysis of fibrin fiber diameter measurement: communication from the ISTH SSC subcommittee on FXIII and fibrinogen. J Thromb Haemost. 2026;24(1):318-328. doi:10.1016/j.jtha.2025.09.013.

19. Mickel W, Münster S, Jawerth LM, et al. Robust pore size analysis of filamentous networks from three-dimensional confocal microscopy. Biophys J. 2008;95(12):6072-6080. doi:10.1529/biophysj.108.135939.
20. Molteni M, Magatti D, Cardinali B, Rocco M, Ferri F. Fast two-dimensional bubble analysis of biopolymer filamentous networks pore size from confocal microscopy thin data stacks. Biophys J. 2013;104(5):1160-1169. doi:10.1016/j.bpj.2013.01.016.
21. Chiu CL, Hecht V, Duong H, Wu B, Tawil B. Permeability of three-dimensional fibrin constructs corresponds to fibrinogen and thrombin concentrations. Biores Open Access. 2012;1(1):34-40. doi:10.1089/biores.2012.0211.
22. Kim OV, Xu Z, Rosen ED, Alber MS. Fibrin networks regulate protein transport during thrombus development. PLoS Comput Biol. 2013;9(6):e1003095. doi:10.1371/journal.pcbi.1003095.
23. Sabra A, Lawrence MJ, Curtis D, Hawkins K, Williams PR, Evans PA. In vitro clot model to evaluate fibrin-thrombin effects on fractal dimension of incipient blood clot. Clin Hemorheol Microcirc. 2019:147-153. doi:10.3233/CH-190615.
24. Berger M, Hell T, Tobiasch A, et al. Analysis of fibrin networks using topological data analysis: a feasibility study. Sci Rep. 2024;14:13123. doi:10.1038/s41598-024-63935-7.
25. Cohen SI, Vendruscolo M, Dobson CM, Knowles TP. Nucleated polymerization with secondary pathways. II. Determination of self-consistent solutions to growth processes described by non-linear master equations. J Chem Phys. 2011;135(6):065106. doi:10.1063/1.3608917.
26. Li W, Sigley J, Baker SR, et al. Nonuniform internal structure of fibrin fibers: protein density and bond density strongly decrease with increasing diameter. Biomed Res Int. 2017;2017:6385628. doi:10.1155/2017/6385628.